Theoretical and Measured Electron-Density Distributions at High Altitudes

SANG-WOOK KANG*
Calspan Corporation, Buffalo, N.Y.

AND

W. LINWOOD JONES†
NASA Langley Research Center, Hampton, Va.

AND

MICHAEL G. DUNN‡
Calspan Corporation, Buffalo, N.Y.

A viscous shock-layer analysis has been developed and applied to the calculation of nonequilibrium-flow species distributions in the plasma layer of a blunt-nosed vehicle at high altitudes. The theoretical electron-density results obtained are in good agreement with those measured in flight for a hemisphere-9° cone entry vehicle. The flight measurements were obtained using electrostatic probes that protruded well into the shock layer. In addition, the theoretically obtained heavy-particle translational temperatures appear to agree fairly well with the electron temperatures that were measured in the flight experiments using voltage-swept thin-wire electrostatic probes. The influence of the reaction-rate coefficients on the calculated electron densities has been assessed and shown to be within the uncertainty in the flight data. The theoretical results demonstrate the importance of including in the chemical model the positive ions N_2^+, O_2^+, N^+, and O^+, in addition to NO^+, for the high altitudes and velocities considered here.

Nomenclature

A = skin-friction parameter, $(\partial U/\partial F)_b$
B = heat-transfer parameter, $(\partial \Theta/\partial F)_b$
C_i = mass fraction of ith species, g_i/g of mixture
C_{p_i} = specific heat at constant pressure of ith species, cal/g_i − °K
D_i = binary diffusion coefficient of ith species, cm^2/sec
E_i = surface-concentration gradient parameter of ith species, $\equiv (\partial C_i/\partial F)_b$
F = transformed normal coordinate, Eq. (10)
f = dimensionless stream function
G = parameter for shock standoff distance, Eq. (10)
H = total enthalpy, $h+(u^2+v^2)/2$, cal/g or atm-cm^3/g
h_i = static enthalpy of ith species, $h_i^0 + \int_0^T C_{p_i}\,dT$, cal/$g_i$
h_i^0 = heat of formation of ith species, cal/g_i
h = static enthalpy, $\sum_i C_i h_i$, cal/g of mixture
j = unity for axisymmetric flow and zero for planar flow
K^2 = rarefaction parameter
Le_i = Lewis number of ith species, Pr/Sc_i
m_i = molecular weight of ith species, g_i/g mole$_i$
n_i = mole fraction of ith species, C_i/m_i, mole$_i$/g of mixture
N_0 = Avogadro's number, 6.025×10^{23}, particles/mole
p = pressure, atm
Pr = Prandtl number
R_C = radius of curvature, cm
R_N = nose radius, cm
$\mathscr{R}$ = universal gas constant, 82.06 atm-cm^3/g mole − °K
r = distance from the axis to the body surface, cm
Sc_i = Schmidt number of ith species
T = temperature, °K
U = dimensionless streamwise velocity, $u/(U_\infty \cos\beta)$
U_∞ = freestream velocity, cm/sec
u, v = velocities in physical coordinates (Fig. 1)
x, y = physical coordinates (Fig. 1)
z = $\equiv r/R_N$
β = shock angle
γ = specific heat ratio
Δ = shock standoff distance, cm
Θ = total-enthalpy ratio, $(H-H_b)/(H_\infty - H_b)$
λ = temperature ratio, T/T_∞
μ = viscosity, g/cm-sec
ξ = dimensionless streamwise distance, x/R_N
ρ = density, g/cm^3
σ_e = electron number density, particles/cm^3
τ_{d_i} = energy of formation of jth species, $h_i^0 m_i/\mathscr{R}$, °K
ψ = stream function
Ω_i = species-concentration integral of ith species—e.g., Eq. (16)

Subscripts

b = body surface
i = ith species
∞ = freestream condition

Received March 7, 1972; presented as Paper 72-689 at the AIAA 5th Fluid and Plasma Dynamics Meeting, Boston, Mass., June 26–28, 1972; revision received July 12, 1972. This research was supported by NASA Langley Research Center, under Contract NAS 1-10674.

Index categories: Viscous Nonboundary-Layer Flows; Thermochemistry and Chemical Kinetics.

* Engineer; formerly Cornell Aeronautical Laboratory Inc.

† Head, Microwave Analysis Section.

‡ Engineer; formerly Cornell Aeronautical Laboratory Inc. Member AIAA.

I. Introduction

FOR hypersonic flight vehicles at high altitudes, the flowfield surrounding the body—i.e., the shock layer—is fully viscous, with the result that the conventional separation of the inviscid layer and the thin boundary layer is not warranted. For example, for a vehicle with a 12-in. nose diameter, a separate analysis is needed at altitudes above 230,000 ft which accounts for the thickened shock-transition zone and the fully viscous fluid within the shock layer along with the effects of chemical nonequilibrium. Analyses are available for the nose region of a blunt

vehicle.[1-4] It is the purpose of this paper 1) to analyze theoretically the multicomponent, ionized, nonequilibrium flow at high altitudes over a sphere-cone vehicle including the afterbody section downstream of the sphere-cone junction; and 2) to compare the theoretical results with available in-flight measurements of electron-density distributions in the plasma layer.

The present analysis represents an extension of the basic treatment developed in Ref. 2 to the case of a body composed of a spherical nose region and a conical afterbody section for which the radius of curvature is infinite. For quantitative results, the extended theory has been applied to a NASA-developed RAM-C vehicle (hemisphere-9° cone) for which large amounts of actual flight data are readily available.[5-12] For low altitudes, these measurements compared well with the theory developed[13,14] from a boundary-layer point of view. At high altitudes, the viscous-layer theory developed in the present paper will be shown to compare favorably with the flight data in terms of the electron-density profiles across the viscous shock layer at the base of the sphere-cone vehicle.

The flight data reported here were obtained as part of the Langley Research Center's Project RAM (Radio Attenuation Measurements) which has for several years conducted in-flight measurements in order to improve understanding of the causes and methods of predicting[13,14] or preventing[5,6] the radio-signal degradation during Earth entry of a space vehicle. Electrostatic probes projecting from the spacecraft into the plasma layer have been flown in an attempt to measure in-flight electron-density distributions.[7,11] Onboard diagnostic antennas,[8] reflectometers,[9] and VHF antennas[10] have also been used to obtain information about the surrounding plasma.

The theoretical analysis will be discussed in Sec. II and followed in Sec. III by a discussion of the chemical model and associated reaction-rate coefficients. The experiment and diagnostic techniques are discussed briefly in Sec. IV. In Sec. V, the theoretical results are compared with the flight data and the influences of uncertainties in the chemical model, and reaction-rate coefficients are assessed.

II. Theoretical Analysis

In order to present the analysis in a self-contained and coherent manner, the major aspects involved in the development of the theoretical analysis will be included here. More complete details may be found in Ref. 2.

The assumptions made in the theoretical analysis are 1) a thin shock layer, 2) the two-layer model of Cheng,[15] 3) constant Prandtl and Schmidt numbers, 4) binary diffusion resulting from concentration gradient only, 5) negligible changes in the pressure, velocity, and total enthalpy resulting from the chemical reactions in the flowfield, and 6) ambipolar diffusion for the electron and ions. These assumptions have been made wholly or in part in the previous analyses, and the justification for these assumptions can be found in Refs. 15–19.

A. Basic Equations

Based on the above assumptions the governing equations for the viscous, ionized shock layer in the merged-layer regime become[2,15]

$$(\partial/\partial x)(\rho u r^j)+(\partial/\partial y)(\rho v r^j)=0 \tag{1}$$

$$\rho u\,\partial u/\partial x+\rho v\,\partial u/\partial y=(\partial/\partial y)(\mu\,\partial u/\partial y) \tag{2}$$

$$\rho(u^2/R_C)=\partial p/\partial y \tag{3}$$

$$\rho u(\partial H/\partial x)+\rho v(\partial H/\partial y)=(\partial/\partial y)\{(\mu/Pr)(\partial/\partial y)[H+(Pr-1)(u^2/2)]\}+(\partial/\partial y)\{(\mu/Pr)(Le_i-1)\sum_i h_i\,\partial C_i/\partial y\} \tag{4}$$

$$\rho u\,\partial C_i/\partial x+\rho v\,\partial C_i/\partial y=w_i+(\partial/\partial y)(\rho D_i\,\partial C_i/\partial y) \tag{5}$$

$$p=\rho\mathscr{R}T\sum_i(C_i/m_i) \tag{6}$$

These equations express the conservation of mass, momentum, energy, and chemical species, respectively, along with an equation of state. (See Fig. 1 for a description of the flowfield.) The eleven chemical species considered are: O_2, N_2, O, N, NO, NO^+, O^+, N^+, O_2^+, N_2^+, and e^-. With the two-layer model of Cheng,[15] these equations are applied to the viscous shock layer allowing for the diffusion of the species into the shock-transition zone by using the modified Rankine-Hugoniot conditions. Analysis of the entire flowfield performed in Ref. 19 reinforces the applicability of the two-layer model, and only the viscous shock layer will be considered here.

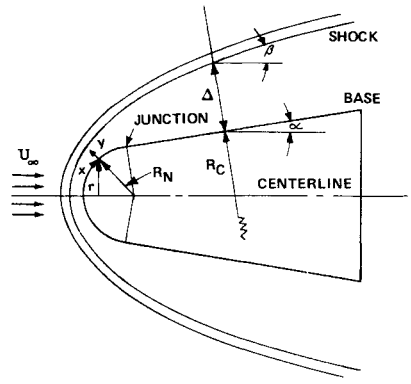

Fig. 1 Schematic flowfield.

B. Boundary Conditions

The boundary conditions for a fully catalytic solid wall are[2,15]:

at $y=0$ $\quad u=0=v,\ H=H_b(x),\ p=p_b(x)$

$$C_i=C_i(\infty) \qquad (O_2,\ N_2) \tag{7}$$

$$C_i=0 \qquad \text{(all other species)}$$

at $y=\Delta(x)$

$$u=U_\infty\cos\beta-(\mu/\rho_\infty U_\infty\sin\beta)(\partial u/\partial y)$$

$$p\cong\rho_\infty U_\infty{}^2\sin^2\beta$$

$$H=H_\infty-(\mu/Pr\rho_\infty U_\infty\sin\beta)(\partial/\partial y)[H+(Pr-1)u^2/2] \tag{8}$$

$$C_i=-(\mu/Sc_i\rho_\infty U_\infty\sin\beta)\,\partial C_i/\partial y \qquad (i\neq N_2,\ O_2)$$

The molecular concentrations are expressed in terms of the other species by locally conserving the elemental composition. In the case of pure air, of present interest, this yields

$$C_{O_2}(y)=C_{O_2}(\infty)-C_O(y)-(m_O/m_{NO})C_{NO}(y)-(m_O/m_{NO^+})C_{NO^+}(y)-C_{O^+}(y)-C_{O_2^+}(y)$$

$$C_{N_2}(y)=C_{N_2}(\infty)-C_N(y)-(m_N/m_{NO})C_{NO}(y)-(m_N/m_{NO^+})C_{NO^+}(y)-C_{N^+}(y)-C_{N_2^+}(y) \tag{9}$$

where $C_{N_2}(\infty)$ is taken to be 0.767 and $C_{O_2}(\infty)=0.233$.

The chemical reactions used simultaneously for dissociation and ionization are given and discussed in detail along with a table in Sec. III. It may be mentioned here that eleven reactions are used involving only neutral species and fifteen reactions for charged species.

C. Method of Analysis

In analyzing the Eqs. (1–6) with the boundary conditions and the chemical reactions, the physical coordinates are transformed as follows[2]:

$$\xi\equiv\frac{x}{R_N} \qquad F\equiv\frac{1}{G}\int_0^y\frac{\rho}{\rho_\infty}\frac{dy}{R_N} \qquad G\equiv\int_0^{\Delta(x)}\frac{\rho}{\rho_\infty}\cdot\frac{dy}{R_N} \tag{10}$$

In addition a stream function ψ is introduced such that $\partial\psi/\partial x=-(1+j)(\pi r)^j\rho v$, and $\partial\psi/\partial y=(1+j)(\pi r)^j\rho u$, which satisfies the continuity equation (1). A dimensionless stream function $f(\xi,F)$ is now obtained by putting $\psi=(1+j)\rho_\infty U_\infty r(\pi r)^j f$, which yields the relationship $\partial f/\partial F=UG\cos\beta/z$, where $U\equiv u/(U_\infty\cos\beta)$.

Transformation of Eqs. (2–5) yields, after some rearrangement: streamwise momentum

$$K^2G\left[G\frac{\partial f}{\partial F}\frac{\partial}{\partial\xi}\left(\frac{z}{G}\frac{\partial f}{\partial F}\right)-(1+j)\frac{dz}{d\xi}f\frac{\partial^2 f}{\partial F^2}-z\frac{\partial f}{\partial\xi}\frac{\partial^2 f}{\partial F^2}\right]=\frac{\partial^3 f}{\partial F^3} \tag{11}$$

normal momentum

$$\partial p/\partial F = (\rho_\infty U_\infty{}^2 z^2 R_N/GR_C)(\partial f/\partial F)^2 \tag{12}$$

energy

$$z\left(\frac{\partial f}{\partial F}\frac{\partial \Theta}{\partial \xi} - \frac{\partial f}{\partial \xi}\frac{\partial \Theta}{\partial F}\right) + \frac{z}{1-t_b}\frac{dt_b}{d\xi}\frac{\partial f}{\partial F}(1-\Theta) - (1+j)\frac{dz}{d\xi} f \frac{\partial \Theta}{\partial F} = \frac{1}{PrK^2G}\left(\frac{\partial^2 \Theta}{\partial F^2}\right) + \frac{Pr-1}{Pr}\cdot\frac{2z^2}{(1-t_b)K^2G^3}\cdot\frac{\partial}{\partial F}\left(\frac{\partial f}{\partial F}\cdot\frac{\partial^2 f}{\partial F^2}\right) \tag{13}$$

species

$$z\left(\frac{\partial f}{\partial F}\frac{\partial C_i}{\partial \xi} - \frac{\partial f}{\partial \xi}\frac{\partial C_i}{\partial F}\right) - (1+j)\frac{dz}{d\xi} f \frac{\partial C_i}{\partial F} = \frac{1}{Sc_i K^2 G}\cdot\frac{\partial^2 C_i}{\partial F^2} + \frac{GR_N}{U_\infty}\cdot\frac{w_i}{\rho} \tag{14}$$

where $Sc_i = \mu/(\rho D_i)$, $t_b = H_b/H_\infty$, $\Theta = (H-H_b)/(H_\infty - H_b)$, and K^2 is the rarefaction parameter due to Cheng.[15] The term G is a measure of the thickness of the viscous shock layer in the transformed plane.

The Eqs. (11–14) should be considered simultaneously with appropriate boundary conditions. However, the previous results obtained, especially those by Chung, Holt, and Liu for the stagnation merged layer, indicate that the flowfield properties such as the pressure, normal velocity, and enthalpy change very little despite the presence of chemical reactions in the flow. In the present study, the fluid dynamics equations, Eqs. (11–13), are decoupled from the species-conservation equations, Eq. (14), in an effort to simplify the analysis.

Thus, the flow properties such as the streamwise velocity, the pressure, and the total enthalpy will be first obtained from Eqs. (11–13), so that they may be used as known inputs to the species-conservation equations. The static temperature, on the other hand, is sensitive to the chemical reactions present in the viscous shock layer, and must be considered along with the species-conservation equations.

Hence, the problem now is to solve simultaneously the species-conservation equation (14) for O, N, NO, NO^+, O^+, N^+, $O_2{}^+$ and $N_2{}^+$. The electron-number density level may be obtained from the relationship $n_e = \sum_k n_k$ (k = ionized species), which gives in particles per cm^3

$$\sigma_e = N_0 \rho C_e/m_e \tag{15}$$

where N_0 is Avogadro's number.

In order to obtain solutions to the present problem, the Kármán-Pohlhausen integral-method approach has been used because of the relative ease of application without unduly sacrificing the accuracy of the results.[2,15,17–20] The method has previously been applied to the case of nonequilibrium flow of binary species by Chung and Anderson,[21] and to merged-layer flows[2,20] with acceptable agreement with the results obtained from other methods. Integrating the species-conservation equations (14) from $F = 0$ to $F = 1$, we obtain, after a series of rearrangements,

$$\frac{d\Omega_i}{d\xi} = z^j\left(\frac{GR_N}{U_\infty}\cdot\int_0^1 \frac{w_i}{\rho}\,dF - \frac{E_i}{Sc_i K^2 G}\right) \tag{16}$$

where

$$\Omega_i \equiv z\cos\beta\cdot G\cdot\int_0^1 UC_i\,dF \quad \text{and} \quad E_i \equiv (\partial C_i/\partial F)_b$$

and i = O, N, NO, NO^+, O^+, N^+, $O_2{}^+$ and $N_2{}^+$.

The various species profiles C_i and the static-temperature profile to be used in the above equations are, for a solid wall (see Ref. 2 for details of derivation):

$$C_i = E_i(F - N_i F^3) \tag{17}$$

and

$$\lambda = \lambda_b + a_1 F + a_2 F^2 + a_3 F^3 \tag{18}$$

where

$$N_i = (1+Q_i)/(3+Q_i), \qquad Q_i \equiv Sc_i K^2 G\sin\beta$$

$$\lambda \equiv T/T_\infty, \qquad \lambda_b = T_b/T_\infty$$

$$a_1 = (1-\lambda_b + U_\infty{}^2/2C_{p\infty}T_\infty)B - (\mathscr{R}/C_{p\infty}T_\infty)\sum_i \tau_{d_i}{}^0 E_i/m_i$$

$$a_2 = -U_\infty{}^2 A^2\cos^2\beta/(2C_{p\infty}T_\infty)$$

and

$$a_3 = 1-\lambda_b + \sin^2\beta U_\infty{}^2 m_\infty(\gamma-1)/[(\gamma+1)\mathscr{R}T_\infty] - a_1 - a_2$$

By substitution of the Eqs. (17) and (18) in the definition of Ω_i along with the other flow properties obtained from Eqs. (11–13), we obtain expressions for these quantities in terms of the unknown parameters E_i. Other terms such as K^2, t_b, G, etc., are specified as known input quantities. Since the species production term w_i contains not only the temperature term but other species terms as well, it is necessary to solve Eq. (16) simultaneously. Thus the problem is to determine from Eq. (16) the unknown parameters E_i as functions of the streamwise distance ξ. The term E_i denotes the local concentration-gradient parameter in the transformed coordinate system. Solutions were obtained by integrating Eq. (16) on a digital computer along the body from the stagnation region through the sphere-cone junction to the afterbody conical section by using the Adams-Molton predictor-corrector method. In order to simplify the analysis while accounting for the change in shock shapes along the body, the distribution of the shock angle was initially assumed and updated from the results. Based on the cases considered in the present analysis, two iterations were usually sufficient to obtain correct shock shape along the body. The solutions are obtained in terms of the flow variables such as the velocity and temperature, and in terms of the chemical species distributions in the shock layer and along the body surface.

III. Chemical Model Used in Analysis

The initial chemical model used in this study was composed of 12 species and 64 chemical reactions. Subsequent calculations performed for the altitude and velocity regime of interest here made it possible to eliminate many of the unimportant reactions from the model. The reaction-rate coefficients were perturbed by factors felt to be consistent with their uncertainty (10 to 100 for many of the ion-atom and ion-molecule reactions) prior to elimination of a particular reaction. The final chemical model used in the analysis is given in Table 1. The model included the neutral species N_2, N, O_2, O, and NO and the charged species $N_2{}^+$, N^+, $O_2{}^+$, O^+, NO^+, and e^-. For the high-altitude conditions of interest here (above 230,000 ft), calculations performed at NASA indicated that ablation-product ionization should not be a problem.

The reaction-rate coefficients for the reactions involving only neutral species (reactions 1–6 and 22–26) have been measured for the conditions of interest and are discussed in Refs. 22–28. The rate coefficients for the deionization of NO^+, O^+, N^+, $O_2{}^+$ and $N_2{}^+$ (reactions 7–10 and 13) have also been measured for the conditions of interest and are reported in Refs. 29–32.

As discussed in Refs. 33–35 the reaction-rate coefficients for the charge-transfer and ion-molecule reactions (reactions 11, 12, 16–20) are not as well known as those for the reactions discussed above. This lack of information is unfortunate because these reactions do play an important part in the nonequilibrium process and can have a significant influence on the relative species distributions. However, for the calculations reported here, the only reactions of this class that were important were reactions 11, 12, and 19. Of these, the rate coefficients for reactions 11 and 12 were used in the data correlation of Refs. 31 and 32 and are felt to be reasonably well known. Perturbation of the rate coefficient of reaction 19 by a factor of 10 will change the relative concentrations of $O_2{}^+$ and NO^+ somewhat but it will not influence the electron density significantly because of the fast two-body dissociative recombination of both NO^+ and $O_2{}^+$. Therefore, even though there is a relatively large uncertainty associated with the reaction-rate coefficient for the ion-atom

Table 1 Chemical reactions and rate coefficients used in nonequilibrium calculations.

NO.	REACTION	FORWARD RATE COEFF, k_F	BACKWARD RATE COEFF, k_B	THIRD BODY, M
	FORWARD DIRECTION	$cm^3/mole\ sec$	$cm^3/mole\ sec$ OR $cm^6/mole^2\ sec$	——
1	$O_2 + M \rightarrow 2O + M$	$3.6 \times 10^{18}\ T^{-1.0}\ \exp(-5.95 \times 10^4/T)$	$3.0 \times 10^{15}\ T^{-0.5}$	N, NO
2	$N_2 + M \rightarrow 2N + M$	$1.9 \times 10^{17}\ T^{-0.5}\ \exp(-1.13 \times 10^5/T)$	$1.1 \times 10^{16}\ T^{-0.5}$	O, NO, O_2
3	$NO + M \rightarrow N + O + M$	$3.9 \times 10^{20}\ T^{-1.5}\ \exp(-7.55 \times 10^4/T)$	$1.0 \times 10^{20}\ T^{-1.5}$	O_2, N_2
4	$O + NO \rightarrow N + O_2$	$3.2 \times 10^{9}\ T\ \exp(-1.97 \times 10^4/T)$	$1.3 \times 10^{10}\ T\ \exp(-3.58 \times 10^3/T)$	
5	$O + N_2 \rightarrow N + NO$	$7.0 \times 10^{13}\ \exp(-3.8 \times 10^4/T)$	1.56×10^{13}	
6	$N + N_2 \rightarrow N + N + N$	$4.085 \times 10^{22}\ T^{-1.5}\ \exp(-1.13 \times 10^5/T)$	$2.27 \times 10^{21}\ T^{-1.5}$	
7	$O + N \rightarrow NO^+ + e^-$	$(1.4 \pm 0.4) \times 10^6\ T^{1.5}\ \exp(-3.19 \times 10^4/T)$	$(6.7 \pm 2.3) \times 10^{21}\ T^{-1.5}$	
8	$O + e^- \rightarrow O^+ + e^- + e^-$	$(3.6 \pm 1.2) \times 10^{31}\ T^{-2.91}\ \exp(-1.58 \times 10^5/T)$	$(2.2 \pm 0.7) \times 10^{40}\ T^{-4.5}$	
9	$N + e^- \rightarrow N^+ + e^- + e^-$	$(1.1 \pm 0.4) \times 10^{32}\ T^{-3.14}\ \exp(-1.69 \times 10^5/T)$	$(2.2 \pm 0.7) \times 10^{40}\ T^{-4.5}$	
10	$O + O \rightarrow O_2^+ + e^-$	$(1.6 \pm 0.4) \times 10^{17}\ T^{-0.98}\ \exp(-8.08 \times 10^4/T)$	$(8.0 \pm 2.0) \times 10^{21}\ T^{-1.5}$	
11	$O + O_2^+ \rightarrow O_2 + O^+$	$2.92 \times 10^{18}\ T^{-1.11}\ \exp(-2.8 \times 10^4/T)$	$7.8 \times 10^{11}\ T^{0.5}$	
12	$N_2 + N^+ \rightarrow N + N_2^+$	$2.02 \times 10^{11}\ T^{0.81}\ \exp(-1.3 \times 10^4/T)$	$7.8 \times 10^{11}\ T^{0.5}$	
13	$N + N \rightarrow N_2^+ + e^-$	$(1.4 \pm 0.3) \times 10^{13} \exp(-6.78 \times 10^4/T)$	$(1.5 \pm 0.5) \times 10^{22}\ T^{-1.5}$	
14	$O_2 + N_2 \rightarrow NO + NO^+ + e^-$	$1.38 \times 10^{20}\ T^{-1.84}\ \exp(-1.41 \times 10^5/T)$	$1.0 \times 10^{24}\ T^{-2.5}$	
15	$NO + N_2 \rightarrow NO^+ + e^- + N_2$	$2.2 \times 10^{15}\ T^{-0.35}\ \exp(-1.08 \times 10^5/T)$	$2.2 \times 10^{26}\ T^{-2.5}$	
16	$O + NO^+ \rightarrow NO + O^+$	$3.63 \times 10^{15}\ T^{-0.6}\ \exp(-5.08 \times 10^4/T)$	1.5×10^{13}	
17	$N_2 + O^+ \rightarrow O + N_2^+$	$3.4 \times 10^{19}\ T^{-2.0}\ \exp(-2.3 \times 10^4/T)$	$2.48 \times 10^{19}\ T^{-2.2}$	
18	$N + NO^+ \rightarrow NO + N^+$	$1.0 \times 10^{19}\ T^{-0.93}\ \exp(-6.1 \times 10^4/T)$	4.8×10^{14}	
19	$O_2 + NO^+ \rightarrow NO + O_2^+$	$1.8 \times 10^{15}\ T^{0.17}\ \exp(-3.3 \times 10^4/T)$	$1.8 \times 10^{13}\ T^{0.5}$	
20	$O + NO^+ \rightarrow O_2 + N^+$	$1.34 \times 10^{13}\ T^{0.31}\ \exp(-7.727 \times 10^4/T)$	1.0×10^{14}	
21	$NO + O_2 \rightarrow NO^+ + e^- + O_2$	$8.8 \times 10^{15}\ T^{-0.35}\ \exp(-1.08 \times 10^5/T)$	$8.8 \times 10^{26}\ T^{-2.5}$	
22	$O_2 + O \rightarrow 2O + O$	$9.0 \times 10^{19}\ T^{-1.0}\ \exp(-5.95 \times 10^4/T)$	$7.5 \times 10^{16}\ T^{-0.5}$	
23	$O_2 + O_2 \rightarrow 2O + O_2$	$3.24 \times 10^{19}\ T^{-1.0}\ \exp(-5.95 \times 10^4/T)$	$2.7 \times 10^{16}\ T^{-0.5}$	
24	$O_2 + N_2 \rightarrow 2O + N_2$	$7.2 \times 10^{18}\ T^{-1.0}\ \exp(-5.95 \times 10^4/T)$	$6.0 \times 10^{15}\ T^{-0.5}$	
25	$N_2 + N_2 \rightarrow 2N + N_2$	$4.7 \times 10^{17}\ T^{-0.5}\ \exp(-1.13 \times 10^5/T)$	$2.72 \times 10^{16}\ T^{-0.5}$	
26	$NO + M \rightarrow N + O + M$	$7.8 \times 10^{20}\ T^{-1.5}\ \exp(-7.55 \times 10^4/T)$	$2.0 \times 10^{20}\ T^{-1.5}$	O, N, NO

and ion-molecule reactions, the electron-density levels and distributions for the particular case reported here are not significantly affected.

Reaction-rate coefficients for reactions 14, 15, and 21 were taken from Ref. 34. These rates are not well known, but, fortunately, these reactions do not have a significant influence on the results so that their uncertainty is unimportant compared with that of several other reactions in the model.

In these calculations, the vibrational and electronic degrees of freedom are assumed to remain in thermal equilibrium with translation while the chemical reactions proceed at finite rates. The free-electron temperature was assumed to be equal to the heavy-particle translational temperature. On the basis of the electron temperatures measured in flight near the base of the vehicle and presented in Sec. V of this paper, this assumption appears to be a reasonable one for the calculations reported here.

IV. Description of Experiment and Diagnostics

The RAM C series of flights was designed to obtain data in the velocity regime of about 25,000 fps where the importance of atomic particle ionization cannot be neglected. For the purposes of this paper, we are concerned with the second (RAM C-II) and final (RAM C-III) flights in this series. During this final flight, water and electrophilic liquid were periodically injected into the plasma layer to reduce the free-electron density level; however, only data obtained in the absence of injection are presented. Many different diagnostic techniques were used on these vehicles, but we will discuss only the electrostatic probe results here because this is the only diagnostic providing a direct measurement of electron-density profiles in the plasma.

The re-entry flight-path angle for these payloads was $-15°$ and both of them were spin stabilized at 3 rpm. The payload geometries were nearly identical and consisted of a 6-in.-radius hemispherical nose followed by a 9° half-angle cone. The RAM C-II nose was covered by a beryllium-cap heat sink during the portion of the entry trajectory of interest here. The RAM C-III had a nose covering of phenolic-graphite charring ablator for heat protection. For both payloads, the conical section was covered with a teflon heat shield.[7]

For the RAM C-II payload eight wire probes were located on the leading edge of the rake so that the last probe extended to a maximum distance of approximately 7 cm into the plasma layer. The collectors were placed so that their longitudinal axis was at 45° to the flow direction and they were biased at a constant negative voltage so as to collect ions. Detailed descriptions of the probe and rake construction and the data reduction

procedure are given in Refs. 7, 11, and 12 and therefore will not be repeated here.

For the RAM C-III payload the rake of constant bias-voltage probes was modified[7,12] in that the number of collectors was increased to 16 and the distance that the final probe extended into the plasma layer was increased from 7 to 14 cm. Other modifications of wedge and sweep angle were also made and are discussed in Refs. 7 and 12. The thermocouple rake was modified[7,12] to include four voltage-swept thin-wire probes located so that their longitudinal axis was approximately aligned with the flow direction. The outer wires extended to a maximum distance of 9.5 cm from the body into the plasma layer. The voltage sweep range, sweep cycle, and data collection procedure are all discussed in detail in Ref. 12.

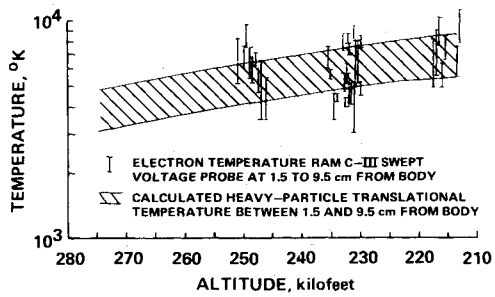

Fig. 3 Comparison between calculated heavy-particle translational temperature and in-flight measured electron temperature.

V. Comparison of Theoretical and Measured Electron Densities

The electrostatic probes discussed in the previous section were used to collect current, from which the electron density could be calculated, from an altitude of approximately 290,000 ft down to 200,000 ft. At this lower altitude, the probes were retracted into the base region but the probes continued to operate and the voltages were recorded. However, for the purposes of this paper, only the electron-density data deduced for the altitude range of 233,000–275,000 ft will be compared with the theoretical results. To test the limitations of the theory, it was applied outside of what is considered the range of validity (due to the neglect of the $\partial p/\partial x$ term as a higher-order term[15] in the present analysis) to calculate profiles for 214,000 ft altitude. Perhaps fortuitously, the calculated results compare favorably with the flight data at this lower altitude as will be shown at the end of this section.

For the altitude range of interest here, the calculated mean free paths were such that the probes were operating in a free-molecular flow environment. It was therefore possible to reduce the voltage-swept thin-wire probe data using the theory of Laframboise[36] and the constant bias-voltage probe data using the theory of Smetana.[37] The accuracy of Laframboise's theoretical results is well known. References 38–40 have demonstrated similarly good results using Smetana's theory. It can be shown that the number densities obtained using the results of Ref. 37 are insensitive to the magnitude of the electron temperature, and this is important from the viewpoint of flight-data analysis. This observation is not generally true when obtaining electron densities from probes aligned with the flow.

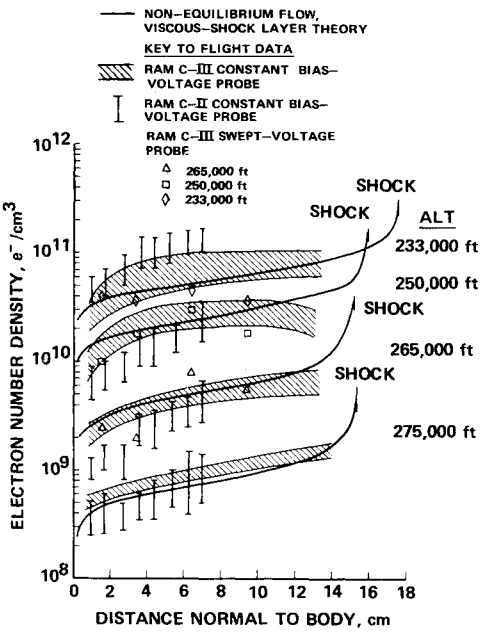

Fig. 2 Comparison between calculated electron density and in-flight electrostatic probe measurements.

Figure 2 illustrates the comparison of the calculated electron densities to those measured, on the C-II and C-III flight experiments, using the electrostatic probes previously described. Comparisons are made for altitudes of 233,000 ft, 250,000 ft, 265,000 ft, and 275,000 ft. At all of these altitudes, the vehicle velocity was approximately constant at a value of approximately 25,100 fps. The trajectories flown by these vehicles are their payload configurations were sufficiently similar that it was not necessary to perform separate calculations for the individual flights. Therefore, both the constant bias-voltage probe data of C-II and C-III and the swept-voltage probe data of C-III are included for comparison purposes. The uncertainty in the flight data obtained with the constant-voltage probes is indicated by the crosshatching and the vertical bars. The data reported are the time-averaged electron densities averaged over one body revolution and the indicated uncertainty represents the peak-to-peak fluctuations mainly due to angle of attack. A similar uncertainty existed in the swept-voltage probe data, but is not illustrated in order to prevent confusion.

The results of the nonequilibrium flow, viscous shock-layer calculations are indicated on Fig. 2 by the solid lines. The shock-layer thickness is also illustrated and shown to decrease with altitude up to approximately 265,000 ft, above which it doesn't appear to change much. The agreement between the calculated electron densities and the flight data is reasonably good over that portion of the shock layer for which data were obtained. The theoretical results show that the electron number-density levels increase near the outer edge of the viscous shock layer. Physically, this seems to be due to the diffusion of the chemical species into the shock-transition zone, giving a finite, non-zero level at the shock-layer edge. In addition, low temperatures exist near the shock-layer outer edge as a result of small shock angle at the base of the vehicle. This means a high level of mass density there, and, coupled with the finite electron-species level, the electron number density is thus seen to increase near the outer edge of the viscous shock layer. However, calculations were performed[41] for a much longer cone of the same nose radius and half-angle. The results show that the peak electron-density levels are located in the plasma layer away from the shock edge, partly due to the thinner, weaker shock existing there.

On the C-III flight the voltage-swept probes were used to make measurements of the electron temperature between 1.5 and 9.5 cm from the body surface. Since the translational temperature was used in the nonequilibrium calculations where, in fact, the electron temperature should have been used for evaluating many of the rate coefficients for reactions involving free electrons, these data are particularly important. The results of the electron-temperature measurements are compared with the calculated heavy-particle translational temperature on Fig. 3. On the basis of this comparison, the electron temperature appears to be approximately equal to the translational temperature at the measuring station. With the available flight data, it is difficult to

be definitive about the relative magnitudes of the heavy-particle temperature and the electron temperature at other locations in the flowfield. However, the flowfields of interest here are highly nonequilibrium and it can be seen from Table 1 that the reaction-rate coefficients for the electron reactions are proportional to the -1.5 to -4.5 power of the electron temperature, suggesting that if there were a substantial difference between the in-flight translational and electron temperatures, it would be reflected in the measured electron densities. It obviously cannot be stated with certainty that such is not the case. What can be said is that if one assumes these two temperatures to be in equilibrium throughout the flowfield, then reasonably good agreement is obtained between data and theory.

The calculations shown on Fig. 2 were obtained using the chemical model given in Table 1. The upper bound of the backward reaction-rate coefficients of reactions 7–10 and 13 were used in this calculation. The values used for the reaction-rate coefficients for the remaining reactions were those given in the table. Because of uncertainties in rate coefficient values, it is important to assess their influence on the calculated electron densities and the subsequent agreement with flight data. This has been accomplished by repeating the nonequilibrium calculations using the lower bound of the backward reaction-rate coefficients of reactions 7–10, and 13 while maintaining those for all other reactions at the Table 1 values. Figure 4 illustrates the results of these calculations for altitudes of 233,000 ft and 275,000 ft. The influence at intermediate altitudes was similar to that shown. The uncertainty in reaction-rate coefficients changes the predicted electron density by a factor of approximately two over the plasma layer. In general, the resulting uncertainty in the calculated number densities is consistent with the uncertainty in the flight data, as can be seen from Fig. 4.

It is also important to assess the influence of the chemical model on the calculated electron densities. Calculations were therefore performed for the probe location using one model in which the only positive ion was NO^+ and a different model in which the positive ions were NO^+, N_2^+, O_2^+, N^+, and O^+. The results of these calculations are illustrated on Fig. 5 for altitudes of 233,000 ft and 275,000 ft. The calculated electron densities at 233,000 ft were found to be essentially uninfluenced by ions other than NO^+. However, at 275,000 ft inclusion of the additional ions in the chemical model drastically influenced the

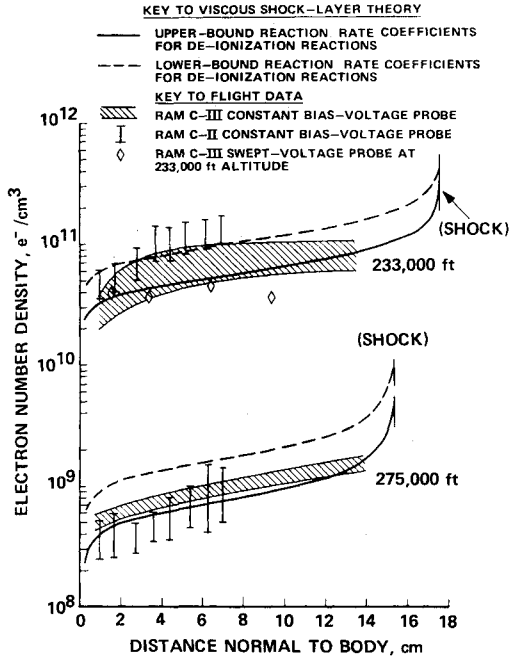

Fig. 4 Influence of reaction-rate coefficients on calculated electron density at electrostatic probe location.

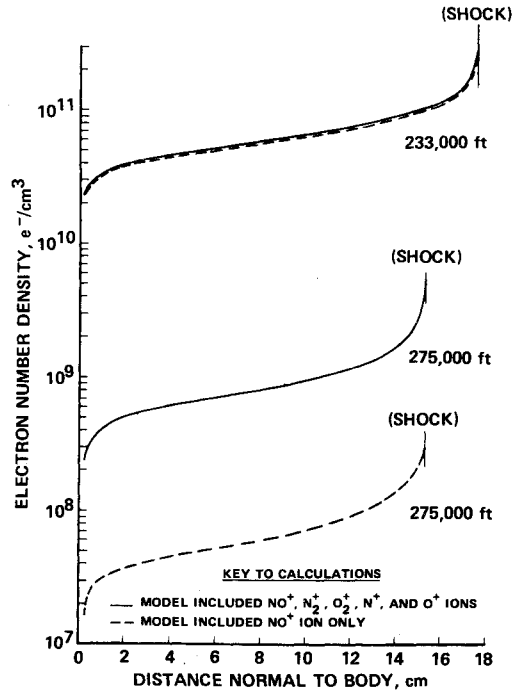

Fig. 5 Influence of chemical model on calculated electron density at electrostatic probe location.

results. It is important to note that the results of the calculation which included only the NO^+ ion fall well below the flight data in contrast to the more complete model which agrees well with flight data. At the probe location, the difference between the calculated results using these two models decreases monotonically in going from 275,000 ft to 233,000 ft.

The electrostatic-probe data were reduced assuming that the mass of dominant ion at the probe location was that of NO^+. Figures 6 and 7 present calculated nonequilibrium species distributions across the plasma layer at the sphere-cone junction and at the probe location for altitudes of 233,000 ft and 275,000 ft. For the probe location and at 233,000 ft, the NO^+ ion is dominant by approximately a factor of ten. However, at the junction the dominant ion was calculated to be O^+. The calculations performed for the 275,000 ft trajectory point indicate that NO^+ was still dominant at the probe location but only by a factor of approximately two. The dominant ion at the junction was again O^+, but NO^+ and O_2^+ were a close second.

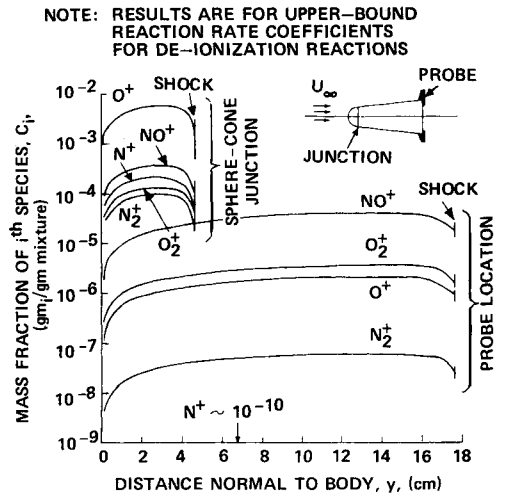

Fig. 6 Nonequilibrium species distributions in plasma layer for 233,000 ft alt at 25,000 fps velocity.

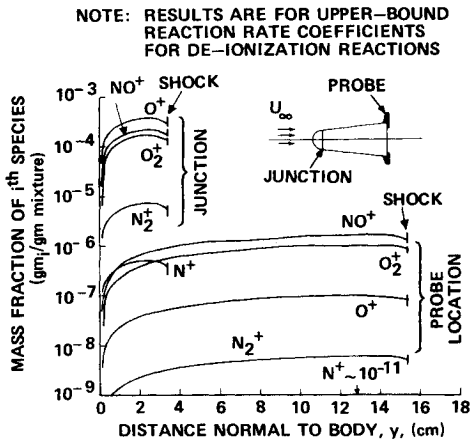

Fig. 7 Nonequilibrium species distributions in plasma layer for 275,000 ft alt at 25,000 fps velocity.

To test the limits of validity of the theory, calculations were performed for a trajectory point at 214,000 ft. At this altitude, conditions are such that theoretically the formulation should not be valid, since the $\partial p/\partial x$ term was neglected in the present analysis as a higher-order term. However, the results of the calculation are shown in Fig. 8 to be in reasonable agreement with the flight data. It is quite possible that this reasonably good agreement at 214,000 ft may be fortuitous. However, the result may be of future interest if one is interested in obtaining an engineering approximation for similar vehicle and trajectory conditions.

In addition to the electrostatic probe data discussed above, flush-mounted microwave reflectometers[9] were also flown on the RAM vehicles. These particular reflectometers can be used to ascertain the electron-density profile in the plasma layer under limited conditions, but they can generally be used to determine the peak value of the electron density at the antenna location. Figures 9 and 10 present favorable comparisons of the predicted electron-density profiles with the peak value of the electron density as determined from the flight data[9] for x/R_N of 5.2 and 7.65 (stations 3 and 4 of Ref. 9), respectively, for altitudes of 233, 250, 265, and 275 kft. Due to the nature of the reflectometers, plasma electron densities beyond y/Δ of 0.8 would not be seen. The agreement between the theoretical results and the flight data is considered to be reasonably good.

Reflectometer measurements were also performed in the nose region at x/R_N of about 0.9 and just after the hemisphere-cone junction at 2.1. However, the agreement between theoretical

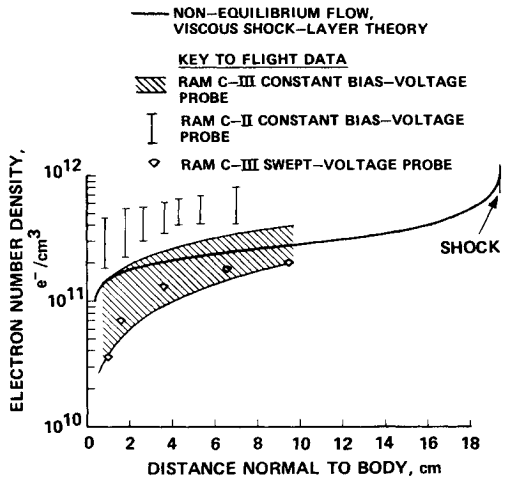

Fig. 8 Comparison between calculated electron density and in-flight electrostatic probe measurements at 214,000 ft alt.

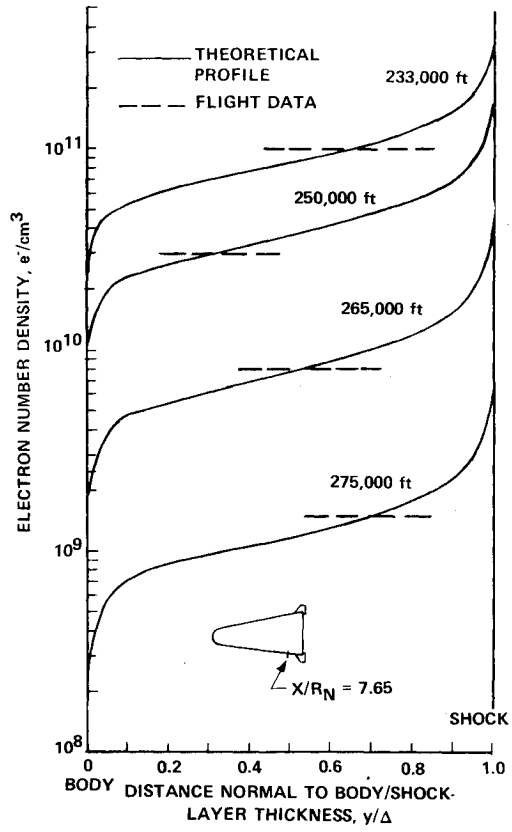

Fig. 9 Comparison of predicted electron density profile with peak value from reflectometer flight data at $x/R_N = 5.2$.

prediction and flight data was not nearly as good for these locations as it was for the two downstream stations. In the nose region, the calculated peak-number density was about 20 times greater than the reflectometer data and at x/R_N of 2.1 the calcu-

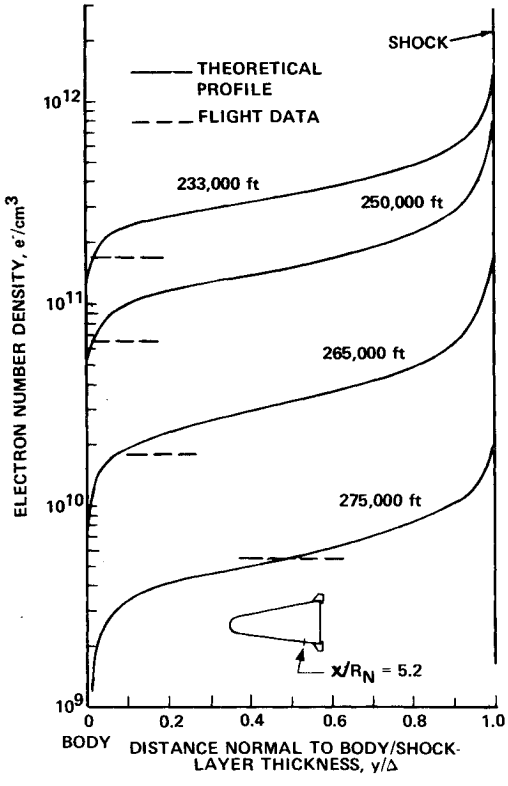

Fig. 10 Comparison of predicted electron-density profile with peak value from reflectometer flight data at $x/R_N = 7.65$.

lated peak value was about 10 times greater than the reflectometer data.

At the present time, the reason for the discrepancy between the reflectometer data at x/R_N of 0.9 and 2.1 and the theoretical prediction is not understood. As possible causes, the translational-vibrational temperature nonequilibrium and the translational-electron temperature nonequilibrium were investigated for an altitude of 265,000 ft. A particular streamline was chosen which enters the viscous shock layer at about 30° from the stagnation line. The results of the calculations of the vibrational-relaxation distance for molecular nitrogen indicated that translational-vibrational equilibrium was achieved in less than 0.8 cm behind the shock. Molecular oxygen would achieve translational-vibrational equilibrium in significantly less distance. It therefore appears reasonable to assume translational-vibrational equilibrium for the viscous hypersonic flow around a RAM-C vehicle at high altitudes. In addition, comparison of the distribution of the electron temperature along the streamline noted above with the nitrogen vibrational temperature and the heavy-particle translational temperature showed that it is appropriate to assume translational-electron temperature equilibrium in the nose region.

VI. Conclusions

In this paper, a multicomponent, ionized, viscous shock-layer flow about a blunt-nosed vehicle (sphere-cone) at high altitudes has been theoretically analyzed. This was accomplished by transforming the coordinates and the flow variables, and by utilizing the Kármán-Pohlhausen integral method to the Navier-Stokes equations and the species-conservation equations under the thin shock-layer assumption.

The theoretical development was applied to a RAM-C sphere-cone vehicle (9° semicone angle), developed by NASA, because of the wealth of in-flight measurements. Eleven chemical species (O_2, N_2, O, N, NO, NO^+, O^+, N^+, O_2^+, N_2^+ and e^-) were included in the analysis for eleven reactions involving only the neutral species and fifteen reactions for charged species. Solutions were obtained at various altitudes where the viscous shock-layer flow exists around the vehicle. The theoretical results for the electron-concentration profiles compare favorably with the experimental data obtained using electrostatic probes located at the base of the vehicle. In addition, the heavy-particle translational temperatures obtained from theory seems to agree fairly well with the electron temperatures measured from the voltage-swept thin-wire electrostatic probes.

The effect of the reaction-rate coefficients on the quantitative theoretical results was also analyzed and shown to be within the uncertainty range of the flight data. The results also demonstrate the importance of including in the chemical model the positive ions N^+, O^+, O_2^+, N_2^+ in addition to NO^+ for high altitudes and velocities considered here.

References

[1] Dellinger, T. C., "Nonequilibrium Air Ionization in Hypersonic Fully Viscous Shock Layers," AIAA Paper 70-806, Los Angeles, Calif., 1970.

[2] Kang, S. W., "Nonequilibrium, Ionized, Hypersonic Flow Over a Blunt Body at Low Reynolds Number," *AIAA Journal*, Vol. 8, No. 7, July 1970, pp. 1263–1270.

[3] Blottner, F. G., "Viscous Shock Layer at the Stagnation Point with Nonequilibrium Air Chemistry," *AIAA Journal*, Vol. 7, No. 12, Dec. 1969, pp. 2281–2288.

[4] Adams, J. C., Jr., "Shock Slip Analysis of Merged Layer Stagnation Point Air Ionization," *AIAA Journal*, Vol. 8, No. 5, May 1970, pp. 971–973.

[5] Akey, N. D. and Cross, A. E., "Radio Blackout Alleviation and Plasma Diagnostic Results From a 25,000 ft/sec Blunt-Body Reentry," TN D-5615, Feb. 1970, NASA.

[6] Schroeder, L. C., "Flight Measurements at 25,000 ft/sec of Plasma Alleviation by Water and Electrophilic Injection," *Proceedings of the Symposium on the Entry Plasma Sheath and its Effects on Space Vehicle Electromagnetic Systems*, NASA, Vol. 2, 1970, pp. 77–100.

[7] Jones, W. L. and Cross, A. E., "Electrostatic Probe Measurements of Plasma Surrounding Three 25,000 ft/sec Reentry Flight Experiments," *Proceedings of the Symposium on the Entry Plasma Sheath and its Effects on Space Vehicle Electromagnetic Systems*, NASA, Vol. 1, 1970, pp. 109–136.

[8] Swift, C. T., Beck, F. B., Thomson, J., and Castellow, S. L., "The RAM C-C S-Band Diagnostic Experiments," *Proceedings of the Symposium on the Entry Plasma Sheath and its Effects on Space Vehicle Electromagnetic Systems*," NASA, Vol. 1, 1970, pp. 137–156.

[9] Grantham, W. L., "Flight Results of a 25,000 ft/sec Reentry Experiment Using Microwave Reflectometers to Measure Plasma Electron Density and Standoff Distance," TN D-6062, Dec. 1970, NASA.

[10] Croswell, W. F. and Jones, W. L., "Effects of Entry Plasma on RAM C-I VHF Telemetry Antennas," *Proceedings of the Symposium on the Entry Plasma Sheath and its Effects on Space Vehicle Electromagnetic Systems*, NASA, Vol. 1, 1970, pp. 183–202.

[11] Jones, W. L. and Cross, A. E., "Electrostatic Probe Measurements of Plasma Parameters for Two Re-entry Flight Experiments at 25,000 ft/sec," TN D-6617, April 1972, NASA.

[12] Schroeder, L. C., Jones, W. L., Swift, C. T., and Cross, A. E., "Radio Blackout Alleviation by Fluid Injection and Plasma Measurements During the RAM C-III Reentry at 25,000 ft/sec," TM X-2563, April 1972, NASA.

[13] Evans, J. S., Schexnayder, C. J., and Huber, P. W., "Computation of Ionization in Reentry Flowfields," *AIAA Journal*, Vol. 8, No. 6, June 1970, pp. 1082–1089.

[14] Huber, P. W., Evans, J. S., and Schexnayder, C. J., "Comparison of Theoretical and Flight-Measured Ionization in a Blunt Body Re-Entry Flowfield," *AIAA Journal*, Vol. 9, No. 6, June 1971, pp. 1154–1162.

[15] Cheng, H. K., "The Blunt-Body Problem in Hypersonic Flow at Low Reynolds Number," AF-1285-A-10, June 1963, Cornell Aeronautical Lab., Buffalo, N.Y.

[16] Probstein, R. F. and Kemp, N., "Viscous Aerodynamic Characteristics in Hypersonic Rarefied Gas Flow," *Journal of the Aerospace Sciences*, Vol. 27, No. 3, March 1960, pp. 174–192.

[17] Lee, R. H. C. and Zierten, T. A., "Merged-Layer Ionization in the Stagnation Region of a Blunt Body," *Proceedings of the Heat Transfer and Fluid Mechanics Institute*, Stanford University Press, Stanford, Calif., 1967, pp. 452–468.

[18] Hayes, W. D. and Probstein, R. F., *Hypersonic Flow Theory*, Academic Press, New York, 1959, pp. 375–395.

[19] Chung, P. M., Holt, J. F., and Liu, S. W., "Merged Stagnation Shock Layer of a Nonequilibrium Dissociating Gas," *AIAA Journal*, Vol. 6, No. 12, Dec. 1968, pp. 2372–2379.

[20] Kang, S. W., "Hypersonic Low Reynolds-Number Flow Over a Blunt Body with Mass Injection," *AIAA Journal*, Vol. 7, No. 8, Aug. 1969, pp. 1546–1552.

[21] Chung, P. M. and Anderson, A. D., "Dissociative Relaxation of Oxygen Over an Adiabatic Flat Plate at Hypersonic Mach Numbers," TN D-140, 1959, NASA.

[22] Hall, J. G., Eschenroeder, A. Q., and Marrone, P. V., "Blunt Nose Inviscid Airflows with Coupled Nonequilibrium Processes," *Journal of the Aerospace Sciences*, Vol. 29, No. 9, Sept. 1962, pp. 1033–1051.

[23] Wray, K. L., "Chemical Kinetics of High Temperature Air," 104, June 1961, Avco-Everett Corp., Everett, Mass.

[24] Appleton, J. P., Steinberg, M., and Liquornik, D. J., "Shock-Tube Study of Nitrogen Dissociation Using Vacuum-Ultraviolet Light Absorption," *Journal of Chemical Physics*, Vol. 48, 1968, pp. 599–608.

[25] Byron, S., "Shock-Tube Measurement of the Rate of Dissociation of Nitrogen," *Journal of Chemical Physics*, Vol. 44, 1966, pp. 1378–1388.

[26] Allen, R. A., Keck, J. C., and Camm, J. C., "Nonequilibrium Radiation and the Recombination Rate in Shock-Heated Nitrogen," *The Physics of Fluids*, Vol. 5, 1962, pp. 284–291.

[27] Cary, B., "Shock-Tube Study of the Thermal Dissociation of Nitrogen," *The Physics of Fluids*, Vol. 8, 1965, pp. 26–35; also *The Physics of Fluids*, Vol. 9, 1966, pp. 1046–1048 for revision.

[28] Wentink, T., Sullivan, J. O., and Wray, K. L., "Nitrogen Atomic Recombination at Room Temperature," *Journal of Chemical Physics*, Vol. 29, 1958, pp. 231–232.

[29] Dunn, M. G. and Lordi, J. A., "Measurement of Electron Temperature and Number Density in Shock-Tunnel Flows. Part II: $NO^+ + e^-$ Dissociative Recombination Rate in Air," *AIAA Journal*, Vol. 7, No. 11, Nov. 1969, pp. 2099–2104.

[30] Dunn, M. G., "Measurement of $C^+ + e^- + e^-$ and $CO^+ + e^-$ Recombination in Carbon Monoxide Flows," *AIAA Journal*, Vol. 9, No. 11, Nov. 1971, pp. 2184–2191.

[31] Dunn, M. G. and Lordi, J. A., "Measurement of $O_2^+ + e^-$

Dissociative Recombination in Expanding Oxygen Flows," *AIAA Journal*, Vol. 8, No. 4, April 1970, pp. 614–618.

[32] Dunn, M. G. and Lordi, J. A., "Measurement of $N_2^+ + e^-$ Dissociative Recombination in Expanding Nitrogen Flows," *AIAA Journal*, Vol. 8, No. 2, Feb. 1970, pp. 339–345.

[33] Wray, K. L., Teare, J. D., Kivel, B., and Hammerling, P., "Relaxation Processes and Reaction Rates Behind Shock Fronts in Air and Component Gases," *Proceedings of the 8th Symposium (International) on Combustion*, The Combustion Inst., Williams and Wilkins, Baltimore, Md., 1960, pp. 328–339.

[34] Dunn, M. G. and Treanor, C. E., "Electron and Ion Chemistry in Flow Fields," *Journal of Defense Research*, Ser. A, Spring 1970, pp. 23–52.

[35] Bortner, M. H., ed., *DASA Reaction-Rate Handbook*, Defense Atomic Support Agency Information and Analysis Center, Santa Barbara, Calif., 1967.

[36] Laframboise, J. G., "Theory of Spherical and Cylindrical Langmuir Probes in a Collisionless Maxwellian Plasma at Rest," UTIAS Rept. 100, March 1966, Univ. of Toronto, Toronto.

[37] Smetana, F. O., "On the Current Collected by a Charged Circular Cylinder Immersed in a Two Dimensional Rarefied Plasma Stream," *Proceedings of the Third Symposium on Rarefied Gas Dynamics*, edited by J. A. Laurmann, Academic Press, New York, 1962, pp. 65–91.

[38] Scharfman, W. E., "The Use of Langmuir Probes to Determine the Electron Density Surrounding Re-Entry Vehicles," NAS 1-3942, June 1965, Stanford Research Inst., Menlo Park, Calif.

[39] Scharfman, W. E. and Bredfeldt, H. R., "Use of the Langmuir Probe to Determine the Electron Density and Temperature Surrounding Re-Entry Vehicles," NAS 1-4872, NASA 66275, Dec. 1966, Stanford Research Inst., Menlo Park, Calif.

[40] Dunn, M. G., "Laboratory Measurements of Electron Density and Electron Temperature with RAM Flight Probes," *Proceedings of the Symposium on the Entry Plasma Sheath and its Effects on Space Vehicle Electromagnetic Systems*, NASA, Vol. 1, 1970, pp. 261–276.

[41] Kang, S. W. and Dunn, M. G., "Hypersonic, Viscous Shock Layer with Chemical Nonequilibrium for Spherically Blunted Cones," AF-3093-A-1, Feb. 1972, Cornell Aeronautical Lab., Buffalo, N.Y.

FEBRUARY 1973 AIAA JOURNAL VOL. 11, NO. 2

Electrode and Gasdynamic Effects in a Large Nonequilibrium MHD Generator

B. ZAUDERER* AND E. TATE†
General Electric Company, King of Prussia, Pa.

An experimental study was performed to determine the factors limiting the power output of a linear, supersonic Faraday generator, having electrodes suspended in the gas flow. The test gases were cesium seeded neon or argon at 2000–4000°K stagnation temperatures and 5–11 Mw thermal power levels. It was observed that the electrode current varies directly with the cesium concentration for electrode current densities of the order of tens of amp/cm^2. The electrode current was nearly independent of electrode temperature and surface area. It was concluded that the electrode conduction was due to the cesium ion flux at the cathode. The gasdynamic characteristics of the generator as deduced from pressure and Mach number measurements were in fairly good agreement with the theory based on the one-dimensional gas conservation equations. At electromagnetic interaction parameters in excess of 0.4, oblique shock waves were detected in the generator. The shock waves did not noticeably influence the power output. At 2150°K, 8.5% of the thermal power was converted to electric power at the external load. An equivalent amount of power was dissipated internally at the electrodes, primarily at the cathode. It is concluded that by using a larger MHD channel or by operating at higher gas pressure, cesium concentrations, and magnetic field strengths, 20% heat to electric conversion ratios should be readily attainable.

1. Introduction

THIS paper reports on the completion of a major phase of a continuing study of the nonequilibrium MHD generator. The study was performed in a large shock tunnel-MHD generator facility[1,2] at thermal power levels of about 10 Mw, at a few atmospheres stagnation pressures and temperatures in the range of 2000°K to 4000°K. The initial study[2] in this facility was performed with pure noble gases in a supersonic MHD generator which had flush mounted, room temperature electrodes. The major conclusion reached in that study[2] was that electrode conduction losses and the effects of oblique shock waves were the two major phenomena limiting the generator power output. It was also observed that the plasma was highly turbulent with an effective Hall parameter of unity and the generator operated in the normal mode in which the current, field and velocity are mutually orthogonal. The next phase of the research effort was aimed at reducing the electrode losses. This was accomplished by constructing a new channel with heated, wire electrodes which were mounted parallel to and 0.6–0.9 cm away from the electrode wall. In addition, cesium seeded, noble gases were used in order to improve the electrode emission and to reduce the operating gas temperature to as low as 2000°K. The initial results of this study have been reported previously.[3] Briefly, the following major results were obtained. It was observed that the electrode current ignition voltage was considerably reduced by placing the electrodes outside the coldest part of the aerodynamic boundary layer. Heating the electrodes to 1600°K increased the current by only 10% over the room temperature results. The average

Received March 10, 1972; revision received September 18, 1972. The authors wish to thank W. Frey and H. Sharp for their assistance in performing the experiments and N. Rasor for his suggestions on the electrode conduction phenomena. This work was supported in part by the Office of Naval Research.

Index category: Plasma Dynamics and MHD; Electric Power Generation Research.

* Manager, MHD Programs. Associate Fellow AIAA.

† Physicist.